Available online at www.sciencedirect.com
SCIENCE DIRECT®
Pergamon
Acta Materialia 51 (2003) 2457–2475
Acta MATERIALIA
www.actamat-journals.com

Comprehensive microstructural characterization and predictive property modeling of plasma-sprayed zirconia coatings

A. Kulkarni [a,*], Z. Wang [a], T. Nakamura [a], S. Sampath [a], A. Goland [a], H. Herman [a], J. Allen [b], J. Ilavsky [bc], G. Long [b], J. Frahm [d], R.W. Steinbrech [d]

[a] *State University of New York, Old Engineering, Room 314, Stony Brook, NY 11794, USA*
[b] *National Institute of Standards and Technology, Gaithersburg, MD 20899, USA*
[c] *University of Maryland, College Park, MD 20742, USA*
[d] *IWV-2: Institute for Materials and Processing in Energy Systems, Forschungszentrum Julich, Germany*

Received 3 September 2002; received in revised form 23 December 2002; accepted 9 January 2003

Abstract

Quantitative microstructure characterization to better understand processing-microstructure-property correlations is of considerable interest in plasma sprayed coating research. This paper quantifies, by means of small-angle neutron scattering (SANS) data, microstructure (porosity, opening dimensions, orientation and morphologies) in plasma sprayed partially-stabilized zirconia (PSZ) coatings, primarily used as thermal barrier coatings. We report on the investigation of the influence of feedstock characteristics on microstructure and establish its influence on the resultant thermal and mechanical properties. The microstructural parameters determined by SANS studies are then assembled into a preliminary model to develop a predictive capability for estimating the properties of these coatings. Thermal conductivity and elastic modulus were predicted using finite element analysis and ultimately compared to experimental values.

Keywords: Plasma sprayed thermal barrier coatings; Small angle neutron scattering; Porosity; Thermal conductivity; Elastic modulus; Finite element model

1. Introduction

Zirconia-based ceramic coatings are widely used for the thermal, oxidation and hot corrosion protection of high temperature components in gas turbines and diesel engines [1,2]. These coatings provide insulation to metallic structures, thus delaying the thermally-induced failure mechanisms that govern the component durability and life [3,4]. The minimum general requirements for an effective ceramic thermal barrier coating (TBC) are recognized to be: (i) low thermal conductivity; (ii) high temperature viability (>1000 °C); (iii) phase stability; (iv) resistance to thermal fatigue and thermal shock; and (v) ease of application [5]. The most

* Corresponding author: Tel.: +1-631-6324511; fax: +1-631-6328440.
E-mail address: anand.kulkarni@sunysb.edu (A. Kulkarni).

1359-6454/03/$30.00
doi:10.1016/S1359-6454(03)00030-2

commonly employed TBC is partially-stabilized zirconia (PSZ), where the stabilizer is generally yttria. This class of ceramic has a very low thermal conductivity, effectively insulating the underlying superalloy substrate (through an oxidation resistant bond coat) from the high temperature environment. For gas turbine applications, the thickness of the TBC is in the range of 125–300 μm.

Plasma sprayed TBCs have been readily employed in these applications [6,7]. The process involves melting of feedstock materials in a plasma plume and rapidly transporting these molten particles to the substrate, where rapid solidification of individual particle occurs upon impingement. Successive build-up of these "splats" results in a layered arrangement in the coating, analogous to a brick-wall-like structure where the splats are entwined in complex arrays [8,9]. This splat-based layered microstructure leads to an intrinsic anisotropy of the coating in the direction perpendicular to the spray direction. The splats are separated by interlamellar pores resulting from rapid solidification of the lamellae, globular pores formed by incomplete inter-splat contact or around unmelted particles, and intrasplat cracks due to thermal stresses and tensile quenching stress relaxation. This unique attribute of the microstructural features contributes to a further decrease in thermal conductivity. The remarkable feature of the TBC is its survivability, both in thermal shock and in the difficult environmental conditions within the gas turbine. The tenacious characteristic of the TBC originates from the porosity, microcracks and the inherent toughness (R-curve behavior) of these ceramics [10–12]. Finite element modeling to study the effects of pore sizes, shapes and orientations on the mechanical properties of plasma sprayed coatings has been attempted [13]. Although numerous studies involving modeling of the evolution of such deposits have been carried out, serious questions remain, which become particularly important when dealing with TBC performance and reliability [14,15].

This paper will explore plasma spraying of TBCs, with special reference to process-related microstructures and imperfections and their resultant influence on the coating properties. Of principal interest will be the anisotropic nature of the deposits, that is, the layers of splats. This is also reflected in the anisotropic array of porosity, which small-angle neutron scattering (SANS) methods have allowed us to distinguish [16–18]. Recent SANS studies on these coatings have been used to resolve and quantify the microstructural features with respect to porosity, dimensionality and orientation information [19]. Finally, through the application of a variety of characterization methodologies, plasma sprayed TBCs can be reasonably well understood, leading to the process-control of microstructure.

2. Experimental procedure

The primary aim of this investigation has been to examine the effect of material feedstock characteristics (such as particle density, size and shape) on the anisotropic void structure, which, in turn, affects the properties of PSZ coatings, in this case mole fraction of 7–8% yttria. Four powders, made by four different manufacturing methods, were investigated. The feedstock characteristics, their origin, particle size distribution and nitrogen sorption (BET)-based surface areas are listed in Table 1.[1]

The different powder morphologies are shown in Fig. 1. The powders made by the F&C method, which involves electric melting of parent ore, solidifying and crushing the ingot, produces angular/polyhedral particles. The SG technique involves wet chemical synthesis, exhibiting spherical/equiaxed morphology (the particles are comprised of sub-μm unit-particles), thus leading to higher surface area. The A&S technique involves agglomeration of powders with binders and subsequent high temperature treatment, producing globular/rough-textured particles. The plasma densified HOSP process, involving spray drying and plasma densification, produces hollow spheres, sometimes nested.

X-ray phase characterization carried of these

[1] Information on commercial products is given for completeness and does not necessarily constitute or imply their endorsement by the National Institute of Standards and Technology.

Table 1
Feedstock characteristics

Powder type	Processing	Manufacturer	Particle size distribution (μm)	Surface area (m^2/g)
Fused and crushed (F&C)	Cast material, subsequently crushed	MSM ZY7∗	10–60	0.08
Sol gel (SG)	Wet precipitation chemical technique	MEL PWA 1375 G	5–50	3.96
Agglomerated and sintered (A&S)	Spray dried and sintered	Metco AE 7216	20–70	0.4
Plasma densified (HOSP)	Plasma flame processed/densified	Metco AE7593	20–120	0.48

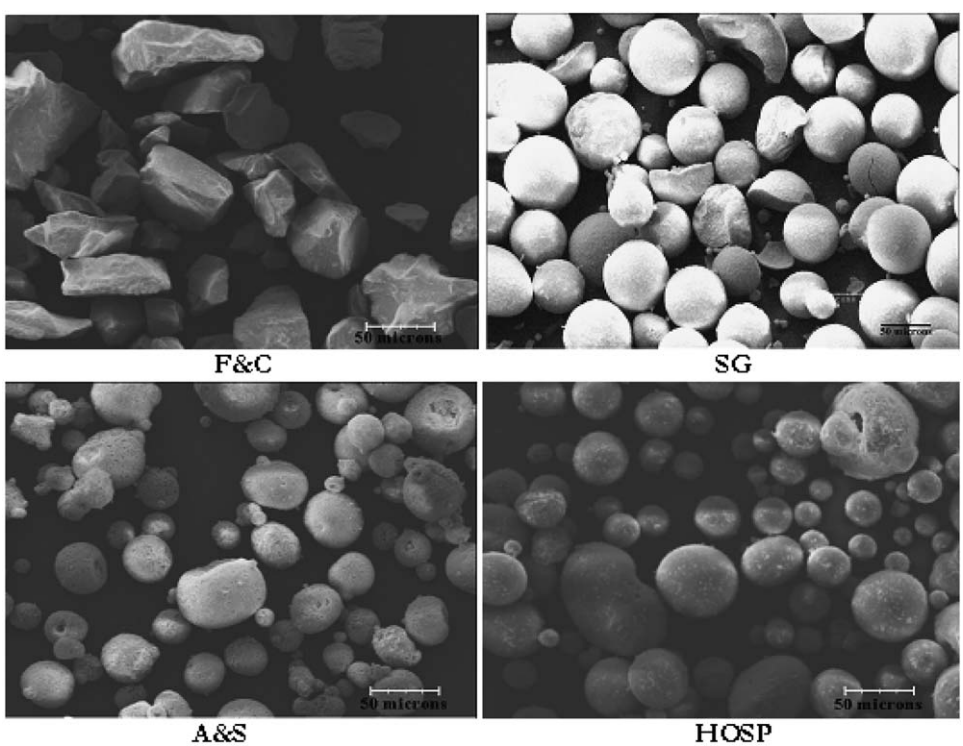

Fig. 1. PSZ powder morphologies observed under SEM (50 μm scalebar).

powders is shown in Fig. 2. Since SG and F&C methods yield uniform chemistry, the only phase detected in these powders is the tetragonal phase, whereas a combination of monoclinic (m) and tetragonal (t) phases, is detected for powders produced by the other two methods. In all samples, the existence of the cubic phase cannot be excluded due to scattering related limitations [20].

Coatings were deposited onto steel substrates using a Sulzer Metco* 3 MB plasma torch, at 100 mm standoff distance. The spray parameters are listed in Table 2. In-flight particle diagnostics were performed using a Tecnar DPV system to monitor particle temperature and velocity, the results of which are shown in Table 3. To understand the effects of process parameters on the droplet substrate interaction, splats were collected on polished stainless steel substrates. Coatings of 1 mm thick-

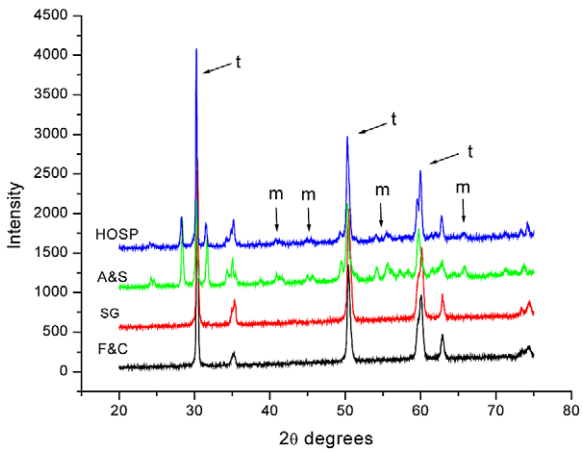

Fig. 2. Phase characterization of powders.

Table 2
Processing parameters for all powders

Parameters	Value
Current (A)	650
Voltage (V)	66–68
Primary gas (SLM)	Argon: 40
Secondary gas (SLM)	Hydrogen: 8
Carrier gas (SCCM)	Argon: 3000
Feed rate (g/min)	20–40
Standoff distance (mm)	100

ness were produced for microstructural characterization and property measurements, whereas 3–4 mm thick coatings were deposited for the SANS studies.

Splats, collected on polished stainless steel substrates, were observed under a white light surface interferometer (Zygo ™*) to quantify the surface profile and the dimensionality of the splats. Free-standing coatings were evaluated for porosity content, property (thermal conductivity and elastic modulus) measurements and SANS studies. Information on porosity was attained using two techniques. Surface-connected porosity was measured by mercury intrusion porosimetry (MIP) using a Quantachrome Autoscan 33* porosimeter. The technique gave an uncertainty of standard deviation ± 3–5% based on the average of 3 measured specimens. The total porosity content (open and closed porosity), used for SANS analysis, was determined using the precision density method, where mass-over-volume ratios were obtained for a cut rectilinear specimen. This technique gives a fractional density (or porosity) uncertainty of standard deviation ± 1% based on the average of 10 measured identical specimens and an assumed theoretical density of 6 g/cm^3. Thermal conductivity measurements were carried out on a 12.5 mm (0.5 inch) diameter disk, coated with carbon, using a Holometrix laser flash* thermal diffusivity instrument. The standard deviation is based on the average of 3 specimens. Phase and microstructural studies were also carried out.

In-plane and out-of-plane elastic modulii were measured for coatings bonded to the substrate. Depth-sensitive indentation measurements were carried out with a Fischerscope 100 C microhardness tester* using a Vickers-type indenter at room temperature (with a maximum load F_{max} = 1 N). An example of a force penetration curve, showing loading (Curve 1) and unloading (Curve 2), is depicted in Fig. 3. The elastic modulus was determined from the elastic recovery part of the force-penetration curve (Curve 3). Curve 3 is a rep-

Table 3
In-flight diagnostics

Powder type	Temperature (°C)	Velocity (m/s)
F&C	2710 ± 300	111 ± 30
SG	2670 ± 300	112 ± 30
A&S	2760 ± 300	125 ± 30
HOSP	2720 ± 300	90 ± 30

(Uncertainties given are standard deviations)

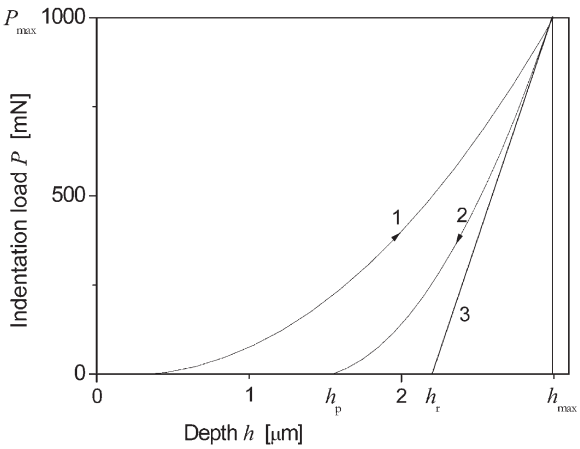

Fig. 3. Force-penetration curve during depth-sensitive microhardness testing. The quantities shown are the depth of indentation at maximum load, h_{max}, the final depth of impression after unloading, h_p, and the intercept of the linear fit, h_r.

resentation of a linear fit to the unloading curve at F_{max} using the equation [DIN ISO 14577].

$$\frac{dF}{dh} = \frac{2}{\sqrt{\pi}} E_r \sqrt{A_r}, \tag{1}$$

where E_r is the reduced elastic modulus

$$E_r = \left(\frac{1-\nu_i}{E_i} + \frac{1-\nu}{E} \right)^{-1}, \tag{2}$$

with the suffix i on the Poisson's ratio ν and E referring to the indenter diamond. Note that the Poisson's ratio of the TBC was assumed to be $\nu = 0.25$. The contact area A_r is related to the impression depth h_r (intercept of the unloading tangent with the abscissa in Fig. 3) by

$$A_r = 26x43xh_r^2, \tag{3}$$

To examine the anisotropy of the various microstructures, measurements were carried out both parallel and perpendicular to the spray direction.

Small-angle neutron scattering studies were carried out on the 8 m SANS instrument at the Cold Neutron Research Facility at the National Institute of Standards and Technology, Gaithersburg, MD [21,22]. In this experiment, a monochromatic beam of thermalized neutrons passes through the specimen in transmission geometry and the scattered neutrons are recorded on a two-dimensional detector; Fig. 4(a). The details of the experiment are described elsewhere [16,19]. The scattering occurs at the void-grain interface due to differences in scattering length density between the material and the pores. The experiment involved two types of measurements, the first being anisotropic Porod scattering. Orientational averaging of the Porod scattering from the sample enables one to obtain the total void surface area per unit sample volume, independent of the precise void morphology. The fine features in the microstructure are major contributors to this deduced surface area. The second type of measurement is anisotropic multiple SANS (MSANS), which involves a measurement of the beam-broadening due to anisotropic multiple scattering by long wavelength neutrons. The multiple scattering usually arises from the coarse features in the microstructure. The MSANS beam-broadening versus wavelength for two sample orientations, with the incident beam out-of-plane (in the spray direction) and in-plane (i.e., in the substrate plane), yields information on microstructural anisotropy. The sector-averaged anisotropic MSANS data also provide microstructural orientation information, as discussed in detail elsewhere [19,23–26].

In Porod scattering, the scattering intensity, $I(Q)$, is a function of the magnitude and direction of the scattering vector, Q, and its orientational average, $<I(Q)>$ is given by:

$$\langle I(Q) \rangle \approx \frac{2\pi |\Delta\rho|^2 S_T}{Q^4}, \tag{4}$$

where, $|Q| = [4\pi/\lambda]\sin\theta$, 2θ is the scattering angle, λ is the wavelength, S_T is the total surface area per unit volume and $|\Delta\rho|^2$ is the scattering contrast between voids and solid matrix; Fig. 4(b). Previously [16–19], it has been shown how the anisotropic Porod scattering can be divided into two anisotropic contributions, one from interlamellar pores that are predominantly parallel to the substrate, the other from intrasplat cracks that are predominantly perpendicular to the substrate. A further isotropic component can be attributed to large globular pores and randomly-oriented irregular voids. However, this Porod scattering contribution is generally too small to be distinguished by anisotropic Porod scattering measurements, alone.

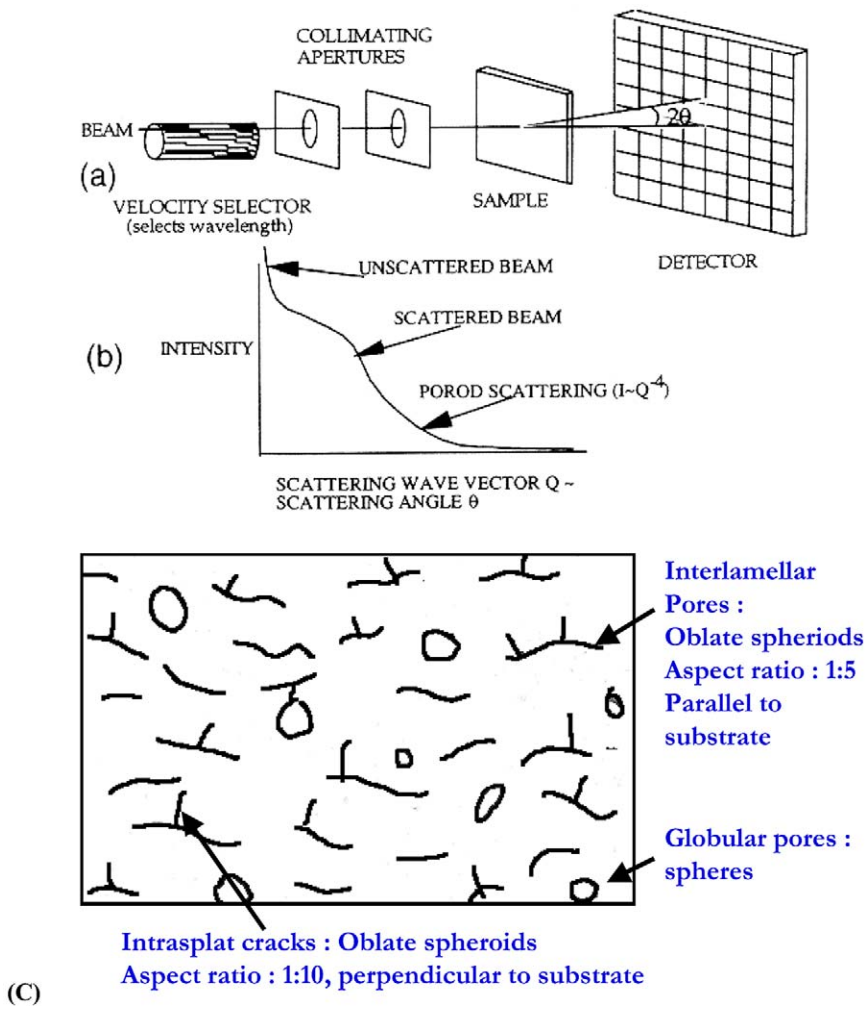

Fig. 4. Experimental setup and scattering intensity curve [16] along with model coating microstructure.

More complete microstructural information was obtained by combining MSANS measurements for different sample orientations, anisotropic Porod surface area distributions, and the total porosity determined from precision density measurements. The MSANS beam-broadening shows much greater sensitivity to the coarse globular and irregular porosity than does the Porod scattering analysis. For interpretation of the anisotropic MSANS beam-broadening data, the interlamellar pores and intrasplat cracks are considered to comprise two space-filling networks of oblate spheroids, each with a fixed aspect ratio, β and the globular pores are considered spheres; Fig. 4(c). While the oblate disc radii of the individual spheroidal elements are almost arbitrary and can be defined for mathematical convenience, the mean opening dimensions, $<$O.D.$>$, for the two populations, together with the associated volume fractions and orientation distributions, and the volume fraction and mean radius of the globular pores, determine the MSANS broadening and anisotropy actually observed. Since the cracks are generally finer than the interlamellar pores, the aspect ratio for the cracks is set to a smaller value (more oblate) than for the interlamellar pores. To acquire a quantitative delineation of the three void components (interlamellar pores, intrasplat cracks and

globular pores) in terms of their porosity contribution, dimensionality and orientation distribution, the following four constraints have to be fulfilled in the MSANS analysis: [19]

1. The component porosities are consistent with the total porosity obtained using precision density measurements.
2. The component surface areas are consistent with the total surface area obtained from anisotropic Porod scattering experiments.
3. The circularly-averaged MSANS beam broadening versus wavelength model predictions are consistent with the experimental data for both orientations: out-of-plane (spray direction) and in-plane (orthogonal direction).
4. The predicted MSANS anisotropy (perpendicular to the substrate) is consistent with that observed experimentally.

With these constraints, it has been possible to determine the volume-weighted mean-opening dimensions of the intrasplat cracks and interlamellar pores, their orientation distributions with respect to the spray direction, and the diameters of the globular pores. Porosity and surface area contributions may also be distinguished.

3. Results and discussions

The experimental SANS results are presented with phase and microstructural characterizations in order to determine the porosity-property relationships. An x-ray phase analysis carried out on the coatings is shown in Fig. 5. All of the coatings show a predominant, non-transformable, tetragonal phase structure as a result of rapid solidification. Again, the results do not exclude the possibility of cubic phase. Fig. 5 also shows that there is a small amount of monoclinic content retained for the coating produced from the HOSP and A&S powders.

SEM microstructures are shown in Fig. 6. Significant differences are observed for each case. While well-adhered splats are observed for the deposit from F&C feedstock, combinations of interlamellar pores, cracks and globular pores are observed for the other coatings. The microstructures also show the columnar structure within the individual splats, which arises from directional heat extraction through the substrate and also from the solidification direction. Interlamellar pores are also visible. These result from poor adhesion between the splats as they accumulate to form the coating. Macroscopically, the coating from the SG feedstock has numerous interlamellar pores compared with the others. The HOSP coating shows larger numbers of unmelted particles owing to the broad powder particle size distribution.

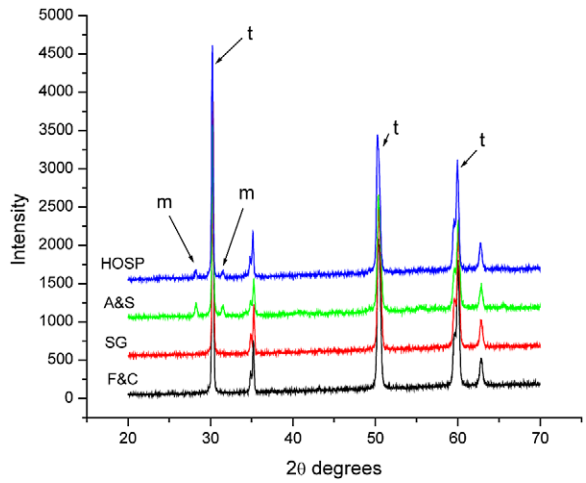

Fig. 5. Phase characterization of coatings.

The measured coating properties, i.e., the porosity from MIP and precision density, the thermal conductivity and the elastic modulus, are listed in Table 4. MIP indicates that there is a considerable variation in the surface-connected porosity for the four cases. The total porosity measured using precision density also shows a wide variation. The porosity for the coating deposited from F&C feedstock is the least porous owing to the splats being well-adhered to one another. This is also consistent with the high thermal conductivity and elastic modulus values for this coating. The coating made from HOSP feedstock shows a significantly lower thermal conductivity and elastic modulus than do the other coatings. This is likely due to its hollow spherical morphology and a broad particle size distribution. There also exists a slight anomaly between results for coatings made from the SG and A&S feedstocks. The SG coating shows lower

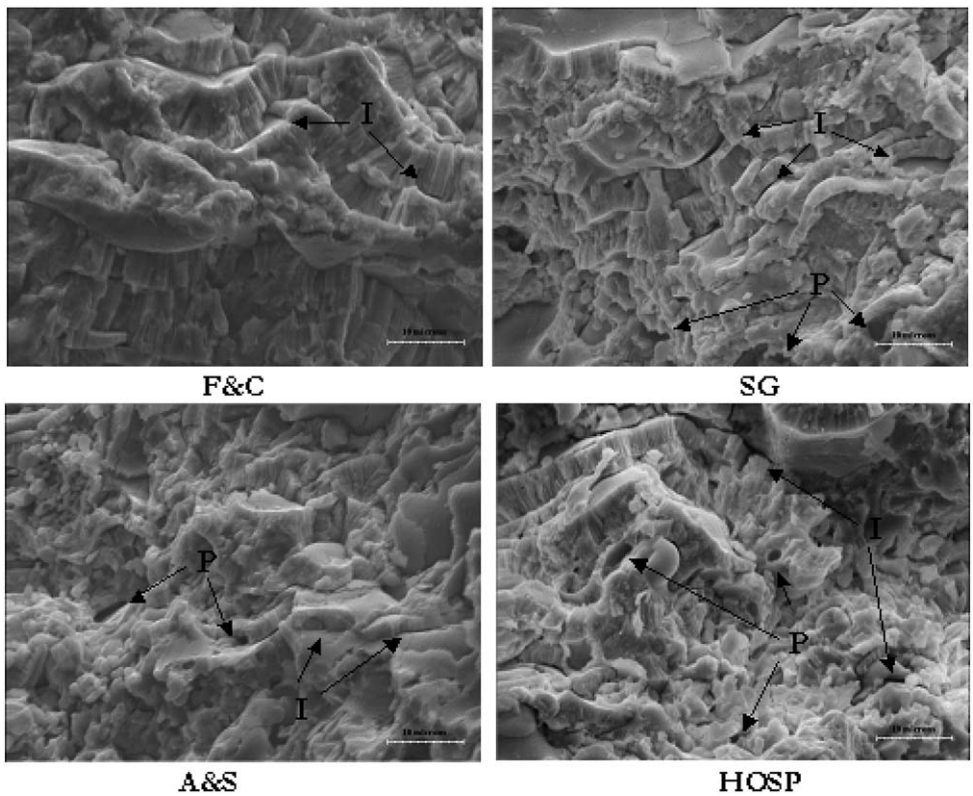

Fig. 6. SEM secondary electron images of fracture cross-sections of the coatings (10 μm scale-bar shown), I – interlamellar pores, P – Globular pores.

Table 4
Coating property measurements

Feedstock	MIP porosity (%)	PD porosity (%)	Th. conductivity (W/m K)	Elastic modulus (GPa)
F&C	7.3 ± 0.4	7.6 ± 0.1	0.95 ± 0.02	76 ± 14
SG	12.5 ± 0.6	13.5 ± 0.2	0.85 ± 0.01	69 ± 17
A&S	14.5 ± 0.7	15 ± 0.2	0.89 ± 0.02	72 ± 20
HOSP	10 ± 0.5	12.2 ± 0.2	0.64 ± 0.01	48 ± 11

thermal conductivity and elastic modulus despite having a lower porosity. Large numbers of interlamellar pores are observed in the SG microstructure, which might explain this anomaly, although further investigation is needed.

For a quantitative evaluation of the microstructures, and a better insight into the property anomalies, SANS measurements were carried out, and the results are given below.

3.1. SANS results

SANS results along with the MSANS model fits are presented in this section. These results include [19] the component porosities of the interlamellar pores and intrasplat cracks, together with their mean opening dimensions and approximate orientation distributions, as well as the porosity of the globular pores and their mean diameter. To model

the intrasplat cracks and interlamellar pores, these are assumed (as in earlier studies [19]) to comprise separate networks of oblate spheroidal elements with aspect ratio values of 1/10 for the intrasplat cracks and 1/5 for the interlamellar pores. Total porosities, measured using the precision density method, and total void surface areas, obtained from a solid-angle averaging of the anisotropic Porod scattering intensity versus Q (Fig. 4(b)), were also used as input for the MSANS model. Fig. 7 shows the MSANS broadening data (r_c in the units of Q) with model-fits (lines) for the coating made from F&C feedstock. The circularly-averaged MSANS broadening, r_c, versus λ for both the sample orientations is shown in Fig. 7(a); Fig. 7(b) shows the anisotropic angular variation of MSANS r_c at different wavelengths in the plane of the spray direction.

The overall MSANS model results for porosity contributions and mean opening dimensions are summarized in Table 5. Estimated standard uncertainties are given in parentheses. The anisotropic orientation distributions of the intrasplat cracks and interlamellar pores (not shown here) are also important in meeting the MSANS model constraints described earlier. The orientation distributions for the interlamellar-pore (β = 1/5) spheroidal elements and the intrasplat-crack (β = 1/10) elements are separately parameterized in terms of the relative probabilities of finding the normal to these elements within the range 0–30° from the spray direction, 30–60° from the spray direction and 60–90° from the spray direction. To obtain MSANS model fits that satisfy all of the constraints, intrasplat cracks are found to be predominantly perpendicular to the substrate (spheroidal-elements normals 60–90° from the spray direction), and the interlamellar pores are found to be predominantly parallel to the substrate (spheroidal-elements normals 0–30° from the spray direction). While the aspect ratios of the spheroidal elements are much milder than the true aspect ratios of the interlamellar pores and intrasplat cracks, the values above suffice for the respective populations of spheroidal voids assumed to form a space-filling network throughout each void system. Indeed, the relatively small area of each spheroidal element permits undulations in the true interlamellar pores and intrasplat cracks to be followed. Furthermore, it is the mean opening dimension, $<$O.D.$>$ = 4 R/3, rather than the oblate disc diameter, 2 R, that is the physical dimension of interest. (In contrast, for the globular voids, the diameter fitted is associated with the actual mean globular pore diameter.) Thus, the $<$O.D.$>$ values of the anisotropic void systems are reported in Table 5, since it is these dimensions that should pertain to actual cracks and pores (of extreme aspect ratios) within the coating microstructure. The results explain the anomaly between the coatings made from the SG and A&S feedstocks. The reduced thermal conductivity and elastic modulus in the SG case can be attributed to a larger amount of interlamellar porosity, despite this system having a lower total porosity. The quantitative separation of the coating microstructure into its components, obtained from the MSANS model results, is shown in Fig. 8.

Table 5 does not reveal why the coating made from HOSP feedstock has such different thermomechanical properties from the other coatings (Table 4). To investigate this and other issues (e.g., the increased number of globular pores for the A&S case) in more detail, the dimensionality of the collected splats was examined for all of the coatings. The splat morphologies are shown in Fig. 9. The disk-shaped splat morphology of the F&C feedstock suggests complete particle melting, resulting in well-adhered splats and consequently a decreased porosity and the higher thermal conductivity and elastic modulus that is observed. While the splats are fragmented in all of the coatings, one reason for the high percentage of globular pores in the coating prepared with A&S feedstock could be the missing cores observed in almost every splat. This could be a result of higher particle velocity during spraying, therefore, less residence time in the plasma and a lower degree of melting. Further investigation is being carried out to determine the extent of melting.

To understand better the correlation between the anisotropy of the microstructure and that of the properties, Table 6 shows the measured elastic modulus both in-plane (parallel to the substrate plane) and out-of-plane (perpendicular to the substrate plane). Given that planar voids perpendicular to the displacement direction depress the elastic

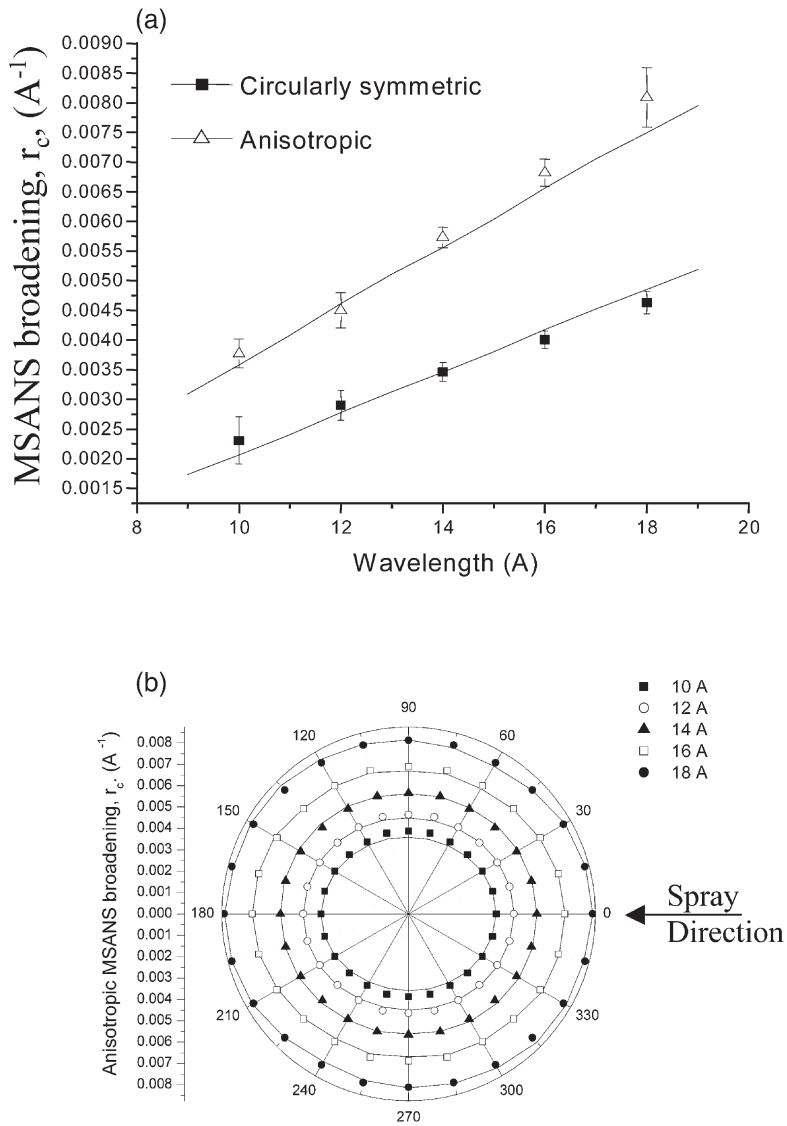

Fig. 7. MSANS broadening experimental data (symbols) with model-fits (lines) for the coating made from F&C feedstock case: (a) MSANS r_c vs λ for both the sample orientations; (b) anisotropic angular MSANS, r_c, at different wavelengths

modulus, the results are consistent with the anisotropies derived from MSANS. Except for the HOSP material, all TBCs show an anisotropy effect. The MSANS results also show a similar proportion of interlamellar pores and intrasplat cracks in the system. The extent of the anisotropy is greatest for the A&S case, consistent with the SANS studies. In the case of anisotropy, the elastic modulus measured perpendicular to the spray direction is 15–20% higher.

Figs 10 and 11 show the porosity–thermal conductivity and the porosity–elastic modulus relationships for the four sprayed materials. Inverse linear dependence of the experimental results of thermal conductivity and elastic modulus are observed with respect to the amount of interlamellar pores,

Table 5
Quantitative MSANS model results

Material	PD porosity (%)	Component porosities (%)			Mean opening dimensions (μm)	Globular pore diameter (μm)
		Interlamellar pores	Intrasplat cracks	Globular pores		
F&C	7.6 ± 0.1	2.1 (2)	2.1 (2)	3.4 (3)	0.053	0.34 (6)
SG	13.5 ± 0.2	4.1 (6)	3.4 (5)	6.0 (6)	0.105	0.68 (6)
A&S	15 ± 0.2	3.8 (5)	2.3 (4)	8.9 (7)	0.108	0.70 (2)
HOSP	12.2 ± 0.2	3.6 (5)	3.4 (5)	5.2 (3)	0.107	0.69 (5)

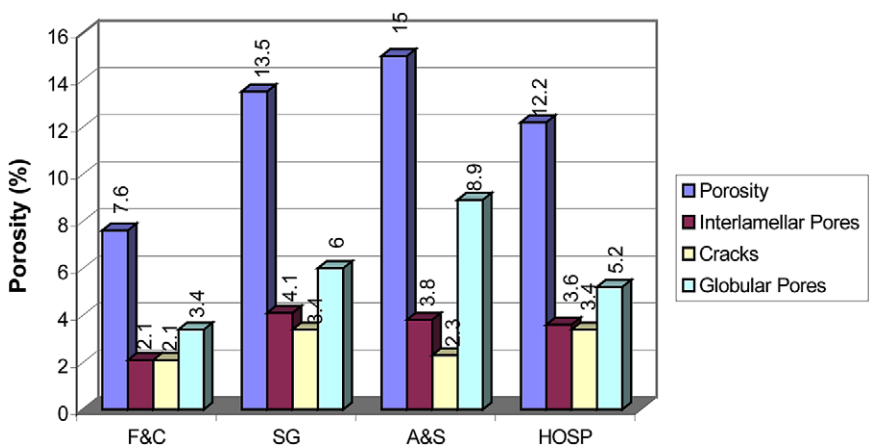

Fig. 8. Quantitative delineation of the coating microstructural features.

obtained from SANS measurements. This suggests that not only do the interlamellar pores play a role in impeding the heat flow in the system, they also provide a cushioning effect for the splats, thus affecting the modulus in a similar way. The results show consistency along these lines for three of the four feedstocks.

The distinctive hollow morphology and broad particle size distribution of the HOSP feedstock powder may be the underlying reason for this coating's lower thermal conductivity and elastic modulus. The dimensions of the splats were measured in an attempt to explain this anomaly of low thermal conductivity and elastic modulus for the HOSP feedstock. Fig. 12 shows splat morphologies for two cases: F&C and HOSP. The table within the figure shows the splat thickness measured in each case. The thickness of the splats is the lowest for the HOSP case, thus resulting in a large number of splat interfaces and leading to a reduction in the thermal conductivity and elastic modulus. It remains unclear as to why this high frequency of splat interface does not manifest itself in either the interlamellar porosity or the surface area of the coating made from the HOSP feedstock.

3.2. SANS-based models

Due to their unique morphology, the thermal and mechanical properties of plasma-sprayed coatings are very different from the properties of the corresponding bulk materials. The existence of pore distributions and splat boundaries significantly reduces the thermal conductivity and elastic modulus of plasma-sprayed PSZ coatings. To estimate the effective properties numerically, two requirements must be satisfied. First, the model sample volume must be large enough to include a rep-

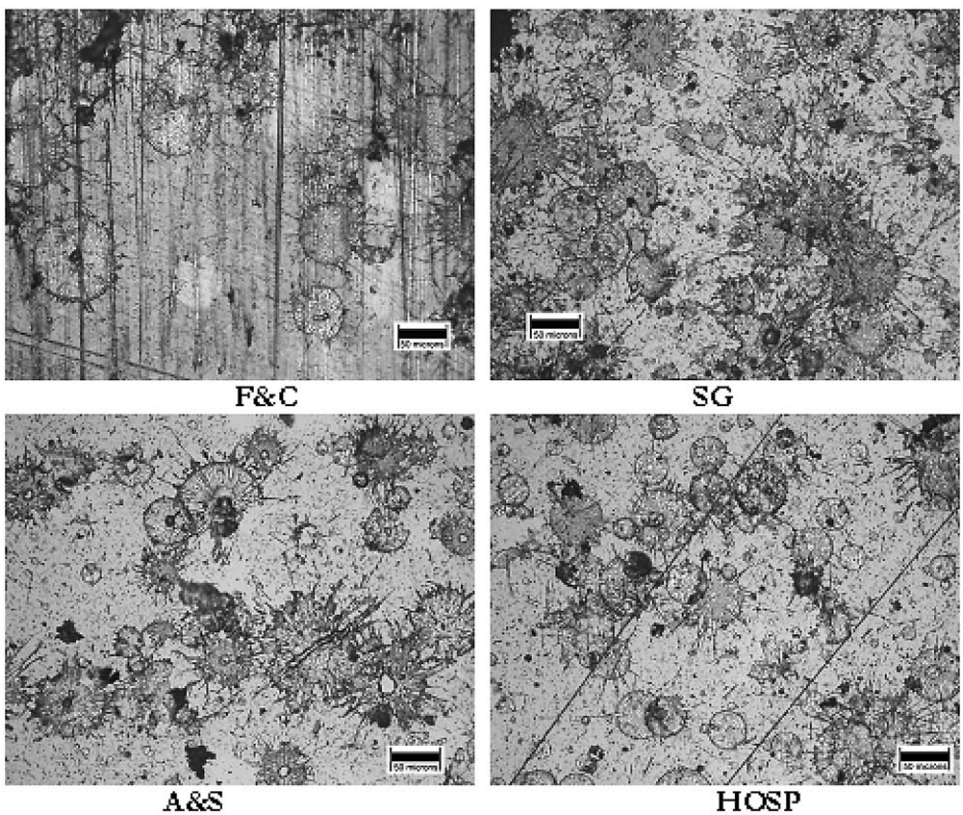

Fig. 9. Single splat morphologies (50 μm scale-bar shown).

Table 6
Values of E-Modulii for in-plane and out-of-plane directions

	F&C		SG		A&S		HOSP	
	E. Modulus [GPa]		E. Modulus [GPa]		E. Modulus [GPa]		E. Modulus [GPa]	
	Perpendicular	Parallel	Perpendicular	Parallel	Perpendicular	Parallel	Perpendicular	Parallel
Average	89	76	80	69	89	72	47	48
Variation	13	14	20	17	21	20	10	11

resentative thermal or mechanical response. If the modeling volume is too small, the numerical results may not be representative due to the stochastic nature of the plasma-spray microstructure, and also because of numerical artifacts introduced at the boundaries. Second, microstructural features must be included in sufficient detail in the model to reflect the real microstructure of the coatings. Various approaches have been taken, such as the Object Oriented Finite Element (OOF) modeling [27], which can be used to quantify real microstructures from images produced by SEM or optical microscopy. In the OOF method, considerable detail, such as voids and impurities, can be

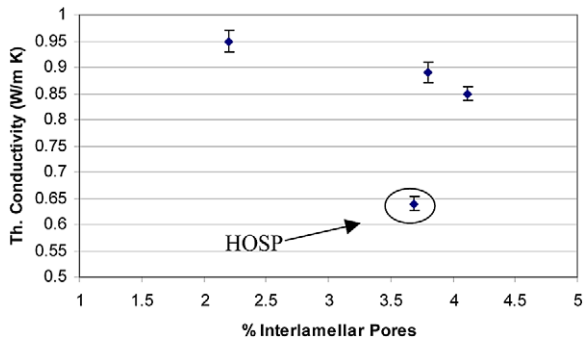

Fig. 10. Porosity–Thermal Conductivity relationships showing the close connection with interlamellar porosity. Vertical bars indicate the statistical standard deviation in the measured thermal conductivity.

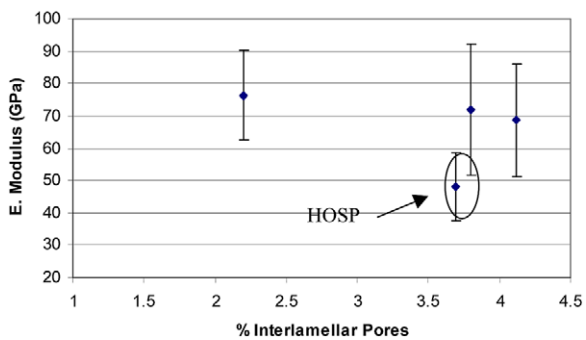

Fig. 11. Porosity–Elastic modulus relationships showing the close connection with interlamellar porosity. Vertical bars indicate the statistical standard deviation in the measured elastic modulus.

included as long as it is clearly visible in the input image. The method has considerable predictive capability based on the empirical 2D representation of real microstructures over a limited sample domain (typically a SEM field-of-view). However, a compromise must usually be made between the smallest sizes resolved and the sample domain size (as controlled by the microscope magnification). Also, problems can arise in interpreting fine anisotropic features that are partly out of the plane of view, particularly if the cracks or planar pores are difficult to detect because of resolution limits. Thus, there is a need for more analytical microstructure models such as that of Kachanov et al. [15]. However such models must include all of the essential microstructure components over the full resolution range of significance, and must be applied over a sufficiently large macroscopic domain to accommodate the stochastic spatial variations in the microstructure present in the actual coating. To address these issues, we have constructed a finite element model, which has both a sufficient resolution and scale of domain, but includes only the most important collective microstructure components, such as total porosity, pore morphology and orientation, etc. To realize this model, volumetrically-averaged MSANS model results were graphically represented in a matrix. A finite element simulation procedure was then used to estimate the effective properties of these coating microstructures.

Following along the lines of the MSANS analysis, we divide the internal voids into three components: interlamellar pores (“Pores”), intrasplat cracks (“Cracks”) and globular or irregular pores (“Voids”). These three components differ in mean size, size distributions, orientation distribution and morphology. However, for the model, all of the pore shapes are idealized to be hexagonal. We assume that the aspect ratio $b/a = 1/10$ (a and b are major and minor axes, respectively) for Cracks, $b/a = 1/5$ for Pores, and $b/a = 0.87$ for Voids, which are here approximated as regular hexagons. Through MSANS analysis, the volume fractions, mean pore dimensions and orientations of the Pores, Voids and Cracks can be determined, as well as the total porosity. These mean opening dimensions closely correspond to the dimensions of the microstructural features in the SEM images of the PSZ coatings. The procedures to build a 2D representation of a 3D axially-symmetric porous model are shown below using the example of the coating produced from the F&C feedstock powder.

First, a domain of 500×300 pixels is considered as shown in Fig. 13(a), which also shows the spray direction. The total porosity in the system and quantitative classification of void components by MSANS, coupled with SEM images of individual features, allows the number of Cracks, Pores and Voids to be calculated, to the (convenient) total of 600 features. Incorporating this volumetrically-averaged information defines a domain large enough to predict stable results with a standard deviation $< 5\%$ [13]. As an example, an illus-

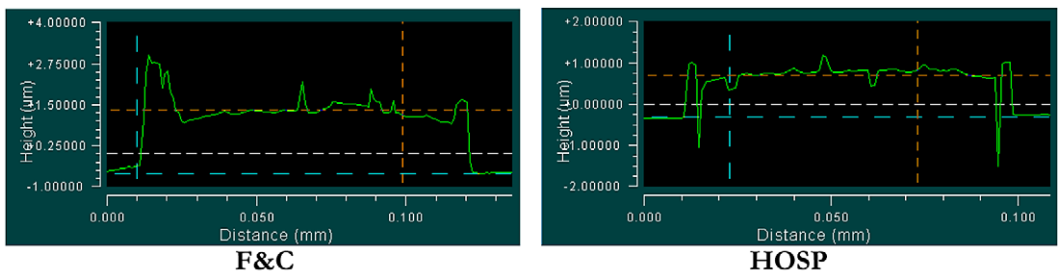

Powder type	Splat thickness (µm)
F&C	1.95 ± 0.3
SG	1.27 ± 0.3
A&S	1.39 ± 0.3
HOSP	1.02 ± 0.2

Fig. 12. Figure shows the surface profile of single splat, the dimensions of which are quantified in the table.

tration of such a calculation for the coating from F&C feedstock is presented. In this system with a total porosity of 7.8%, calculations show 375 Cracks, 190 Pores and 35 Voids to be present. The second step is to generate the geometric model, as shown in Fig. 13 A. Given the dimensions of these void systems, the resolution on the model is zoomed to present the actual components, in this case 0.01 µm/pixel. Feature locations are chosen randomly, while the orientation distributions of Pores and Cracks are each defined by the orientational probabilities obtained from the MSANS analysis of the real microstructure as shown in Table 7. Estimated uncertainties are given in parentheses. In this case, 289 Cracks are placed with the normal to the crack between 60–90° from the spray direction (normal to the coating), 85 Cracks have their normal between 30–60° from the spray direction, and so on. The exact value of the orientation (ϕ) is still randomly determined within the specific ranges. Finally, a random finite element mesh is generated, as shown in Fig. 13(b). 11500 4-noded elements are used in this model. Similarly, computational models of the other three coating systems are constructed. Although these 2D models do not directly reflect the exact microstructure of the coatings, they do include the averaged geometric features of the porous structures.

Steady state heat transfer analyses were carried out to calculate the effective thermal conductivity for both the spray direction and the transverse direction of the four coating systems. For the analysis of the vertical direction (i.e. the spray direction), a fixed temperature is prescribed for both the top and the bottom boundaries, and the other two boundaries are considered as isolated boundaries, as shown in Fig. 14. An effective thermal conductivity in the spray direction can be determined from the following equation,

$$K_{eff} = \frac{QL}{W\Delta T}, \tag{5}$$

where K_{eff} is the effective thermal conductivity, Q is the total heat flux in the spray direction across a transverse model cross-section, W and L are the width and height of the domain, and ΔT is the temperature difference between the top and bottom boundaries. Note that Q is constant for any transverse cross-section in a steady state analysis. The effective thermal conductivity in the transverse direction can be calculated in a similar fashion. Table 8 shows the calculated results for the four systems.

Fig. 14 shows the calculated heat flux in the spray direction for the coatings prepared from the F&C feedstock powder. It is clearly seen that there are concentrations of heat flux between neighboring pores. Thus, the presence of pores narrows the

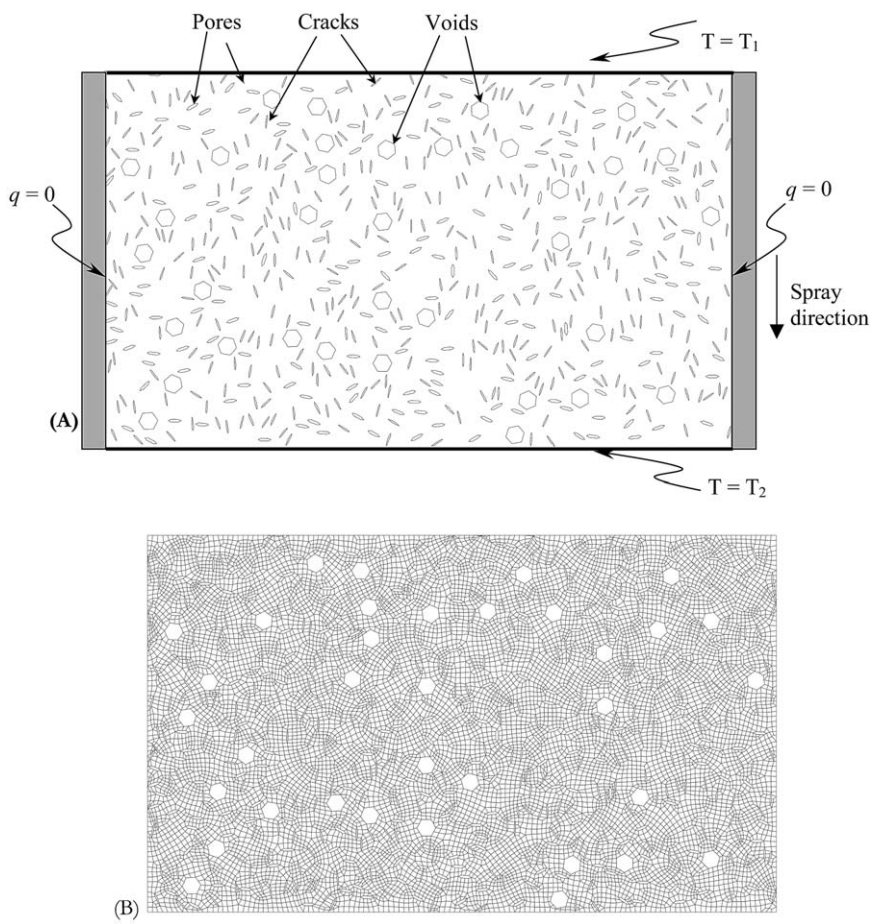

Fig. 13. Computational model of the F&C coating system, with a domain size of 500 × 300 pixels. (a) Randomly distributed pores, grouped into three types: Cracks, Pores and Voids, with fixed temperatures T_1 and T_2 along the top and bottom boundaries The heat flux $q = 0$ indicates no heat loss across boundaries. (b) Finite element mesh, 11500 elements are used.

Table 7
Distributions and morphologies of pores in F&C PSZ coating

	Number of features				*b/a*	*a* (μm)	*b* (μm)
	$0° \leq \phi \leq 30°$	$30° \leq \phi \leq 90°$	$60° \leq \phi \leq 90°$	Total			
Crack	1	85	289	375	1/10	0.26(6)	0.02(7)
Pore	168	13	9	190	1/5	0.26(6)	0.05(3)
Void				35	1/1.15	0.34(7)	0.30(2)

(total porosity is 7.88%)

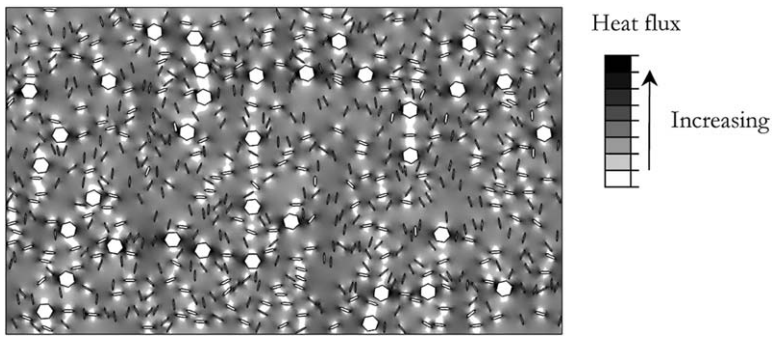

Fig. 14. Contour of heat flux in the spray direction for the coating made from F&C feedstock. Darker areas have higher heat flux.

Table 8
Effective thermal conductivities of the four systems (K_m = 2 W/mK)

	F&C	SG	A&S	HOSP
K_L (W/mK)	1.62	1.37	1.35	1.42
K_T (W/mK)	1.55	1.31	1.35	1.34

path of heat transfer and this reduces the effective thermal conductivity.

Fig. 15 shows the effective thermal conductivities for the four systems, each normalized to the bulk thermal conductivity, K_m. Here, K_L and K_T are the thermal conductivity in the spray direction and in the transverse direction, respectively. As shown, both K_L and K_T decrease with increased total porosity. The ratio of the effective conductivity to the bulk conductivity (2 W/m K) ranges from 66–80%. The PSZ coating prepared from F&C feedstock has the lowest porosity in the four systems, and the highest effective conductivity. The coatings from SG and A&S feedstocks have lower conductivities due to higher porosities. The results show that the effective thermal conductivities are slightly higher in the spray direction than in the transverse direction, except for the A&S case. This trend can probably be explained by the orientation distributions of the Cracks. Most Cracks tend to be oriented close to the vertical direction (i.e., crack normals are nearly in the substrate plane). This causes a higher thermal resistance to the heat flux in the horizontal direction. Although the orientation distribution of the interlamellar pores is the reverse from that for Cracks, the total number of Cracks is much higher than that of Pores, except for the A&S case. This results in a higher overall resistance of heat flux in the transverse direction. However, the difference in the effective thermal conductivities in the two directions is actually quite small. The largest difference is about 6%, which is found in the model of the coating prepared from HOSP feedstock.

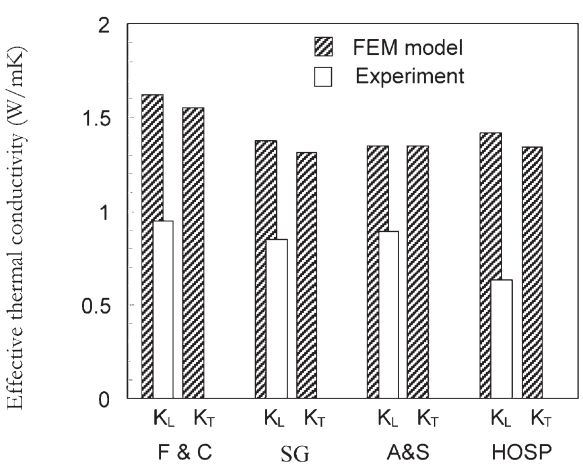

Fig. 15. Comparison of calculated and experimental results of effective thermal conductivity for the four coating systems.

The computed effective thermal conductivities (Table 8) are higher than those measured experimentally. One reason for this difference may be the effect of the splat boundaries, which are expected to have a considerable effect on the heat transfer, and are neglected in our models. Information about the properties of these splat boundaries is being investigated using TEM. On the other hand, mean opening dimensions and fixed aspect ratios are used for each group of pores. In the computational results, the thermal conductivity in the spray direction K_L is slightly higher than that in the perpendicular direction, K_T (except for A&S PSZ), while in experimental results, K_T is higher than K_L. This difference also reveals the important role of splat boundaries and pore size information in the thermal transport and modulus properties. Most splat boundaries and interlamellar pores are perpendicular to the spray direction, therefore, they should cause a greater decrease in K_L than in K_T.

The effective elastic modulii of the four systems were also calculated using the same model. The results are shown in Table 9 and Fig. 16. It is seen that the effective modulus also decreases for both directions when the total porosity increases. The ratio of effective modulus to the bulk modulus, which is around 200 GPa, ranges from 50–70%. The calculated results are higher than the experimental results for all the systems. Again, the main reason is that the splat boundaries and the pore size distribution are both neglected. These have an important influence on the overall modulus of coatings. Also, for the same reason, the calculated modulus in the spray direction E_L is higher than that in the transverse direction E_T.

The results show the effectiveness of a SANS-based computational approach for estimation of the effective materials properties of thermally sprayed PSZ coatings. This method can deal with the large model domain needed to obtain consistent properties, and the major microstructural features can be incorporated into the model. In SANS-based modeling, there are also some limitations, such as the absence of splat boundary information and neglect of the pore size distribution. Differences between calculated and experimental results are caused by these model limitations. Future efforts are underway to minimize these differences by modifying our models.

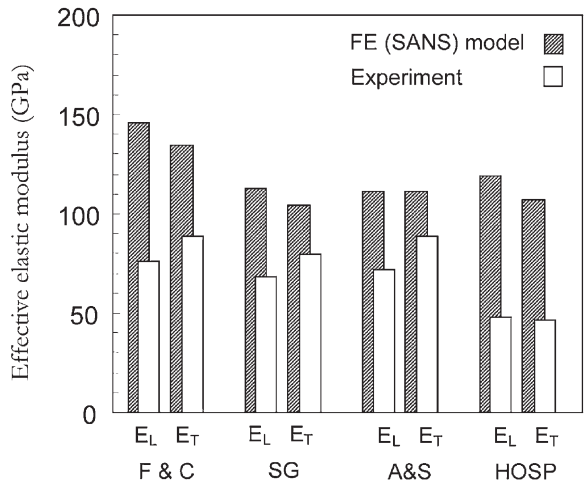

Fig. 16. Comparison of calculated and experimental results of effective elastic modulus for the PSZ coatings.

4. Conclusions

A quantitative characterization of the microstructural features has been demonstrated successfully in the case of plasma sprayed PSZ coatings, using a combination of anisotropic Porod scattering and MSANS scattering techniques. The representation of these microstructural features with respect to their absolute porosities, mean opening dimensions and orientation distributions in a large

Table 9
Effective elastic modulus of the four systems (E_m = 200GPa)

	F&C	SG	A&S	HOSP
E_L (GPa)	145.8	112.8	111.0	119.2
E_T (GPa)	134.6	104.2	111.4	107.4

domain permits the development of a predictive capability in estimating the properties of these coatings. A finite element based model has been successfully developed to realize these volumetrically averaged SANS results.

In this paper, the influence of feedstock characteristics (particle density, size and shape) on the anisotropic void structure has been quantified to establish the processing-microstructure-property relationships. These results are correlated with thermal conductivity and elastic modulus measurements, the properties most sensitive to these microstructural features. Of the four feedstocks studied, the FC feedstock has the highest density of all the powders, thus the highest thermal conductivity and elastic modulus. It is observed that despite higher porosity, the coating made from the A&S feedstock shows higher thermal conductivity and elastic modulus than the SG feedstock. This is explained through quantitative separation of void components from the SANS results where the A&S coating has globular porosity as major constituent to porosity. Thus correlation with percent interlamellar porosity content explains the anomaly in the two systems. Another important result is derived for the case of technologically relevant HOSP feedstock. This feedstock, in spite of superior melting in the plasma (low porosity), exhibits low thermal conductivity and elastic modulus. While the SANS results present some insight to explain this behavior, the single splat studies lead to the existence of a large number of splat interfaces in this coating. This may be attributed to the distinctive hollow particle morphology resulting in thin splats. TEM studies to support these results are underway. Thus, the SANS results, together with the corresponding single splat studies, explain coating properties and some anomalies in the porosity-thermal conductivity and porosity-elastic modulus results.

A finite element based simulation procedure, developed from the volumetrically averaged information of the representative microstructural features (in particular, the porosities, mean opening dimensions and orientation distributions) is presented. The preliminary results of estimated thermal conductivity and elastic modulus show the effectiveness of this SANS based computational approach. The calculated results differ from the experimental results due to lack of information on the splat boundaries and pore size distribution. Transmission electron microscopy studies are underway to investigate further the details of the splat boundaries. Thus, the SANS-based model offers a means for correlating processing with and microstructure properties, a key to predicting, as well as increasing, TBC durability.

Acknowledgements

This research was supported by the National Science Foundation MRSEC program at the SUNY Stony Brook under the Grant No. DMR-0080021. The authors also wish to thank J. Barker and C. J. Glinka of the NIST Center for Neutron Research for scientific and technical support.

References

[1] Miller RA. Surf and Coat Tech 1987;30:1.
[2] Brindley WJ, Miller RA. Adv Mat and Proc 1989;8:29.
[3] Meier SM, Gupta DK. J Eng Gas Turbines Power 1994;116:250.
[4] DeMasi-Marcin JT, Sheffler KD, Bose S. J Eng Gas Turbines Power 1990;112:521.
[5] Jones RL. Thermal barrier coatings. In: Stern KH, editor. Metallurgical and protective coatings. London: Chapman and Hall; 1996. p. 194.
[6] Mannsmann W, Grunling HW. J Phys IV 1993;3:903.
[7] Nelson WA, Orenstein RM. J. Thermal Spray Technol. 1997;6(2):176.
[8] Herman H. Sci American 1988;259(3):112.
[9] McPherson R. Thin Solid Films 1981;83:297.
[10] Pawlowski L, Fauchais P. Int Mater Rev 1992;37:271.
[11] Swain MV, Johnson LF, Syed R, Hasselman DPH. J Mats Sci Lett 1986;5:799.
[12] Vassen R, Tietz F, Kerkhoff G, Wilkenhoner R, Stoever D. In: Lecomte-Beckers J, Schubert F, Ennis PJ, editors. Proceedings of the 6th Liege conference, Part III, Materials for Advanced Power Engineering. Julich: Forschungszentrum Julich GmbH; 1998. p. 1627.
[13] Nakamura T, Qian G, Berndt CC. J Am Ceram Soc 2000;83(3):578.
[14] McPherson R. Thin Solid Films 1984;112:89.
[15] Sevostianov I, Kachanov M. Acta Mater 2000;48:1361.
[16] Ilavsky J, Allen AJ, Long GG, Krueger S, Berndt CC, Herman H, Am J. J Am Ceram Soc 1997;80:733.
[17] Ilavsky J, Allen AJ, Long GG, Berndt CC. Mater Sci Eng A 1999;215:272.

[18] Ilavsky J, Allen AJ, Long GG, Berndt CC, Herman H. J Mater Sci 1997;32:3407.
[19] Allen AJ, Ilavsky J, Long GG, Wallace JS, Berndt CC, Herman H. Acta Mater 2001;49:1661.
[20] Ilavsky J, Stalick JK. Surf and Coat Tech 2000;127:120.
[21] Glinka CJ, Rowe JM, LaRock JG. J Appl Cryst 1985;19:427.
[22] Hammouda B, Krueger S, Glinka CJ. J Res Natl Inst Stand Technol 1993;98:31.
[23] Kostorz G. In: Kostorz G, editor. Treatise on Materials Science and Technology, Vol. 15. New York: Academic Press; 1979. p. 227.
[24] Porod G. In: Glatter O, Kratky O, editors. Small Angle X-ray Scattering. New York: Academic Press; 1982. p. 17.
[25] Allen AJ, Berk NF. J Appl Cryst 1994;27:878.
[26] Allen AJ, Berk NF. Neutron News 1998;9.2:13.
[27] Langer SA, Fuller Jr. ER, Carter WC. Computing in Sci Eng 2001;3(3):15.